2018-09

LOW-FREQUENCY ACOUSTIC VECTOR FIELD STABILITY IN THE PRESENCE OF ENVIRONMENTAL VARIABILITY

Laksana, Fahmi Chandra

Monterey, CA; Naval Postgraduate School

NAVAL POSTGRADUATE SCHOOL

MONTEREY, CALIFORNIA

THESIS

LOW-FREQUENCY ACOUSTIC VECTOR FIELD STABILITY IN THE PRESENCE OF ENVIRONMENTAL VARIABILITY

by

Fahmi Chandra Laksana

September 2018

Thesis Advisor:	Kevin B. Smith
Second Reader:	John E. Joseph

THIS PAGE INTENTIONALLY LEFT BLANK

REPORT DOCUMENTATION PAGE			*Form Approved OMB No. 0704-0188*

1. AGENCY USE ONLY *(Leave blank)*	**2. REPORT DATE** September 2018	**3. REPORT TYPE AND DATES COVERED** Master's thesis

4. TITLE AND SUBTITLE LOW-FREQUENCY ACOUSTIC VECTOR FIELD STABILITY IN THE PRESENCE OF ENVIRONMENTAL VARIABILITY	**5. FUNDING NUMBERS** RPM3A
6. AUTHOR(S) Fahmi Chandra Laksana	
7. PERFORMING ORGANIZATION NAME(S) AND ADDRESS(ES) Naval Postgraduate School Monterey, CA 93943-5000	**8. PERFORMING ORGANIZATION REPORT NUMBER**
9. SPONSORING / MONITORING AGENCY NAME(S) AND ADDRESS(ES) ONR, Monterey, CA 93940	**10. SPONSORING / MONITORING AGENCY REPORT NUMBER**

11. SUPPLEMENTARY NOTES The views expressed in this thesis are those of the author and do not reflect the official policy or position of the Department of Defense or the U.S. Government.

12a. DISTRIBUTION / AVAILABILITY STATEMENT Approved for public release. Distribution is unlimited.	**12b. DISTRIBUTION CODE** A

13. ABSTRACT (maximum 200 words)

The Department of Physics at the Naval Postgraduate School recently collected data from a low-frequency vector sensor system off the coast of Big Sur, California, in May 2018. During the test, signals from numerous surface craft were recorded. In this study, a numerical model was employed to estimate the vector field transmission loss at low frequency in order to estimate performance of the system during the test. In order to provide realistic ranges of values, the impact of environmental variability was examined and the primary factors affecting transmission loss were identified. The range-dependent environmental features included varying bathymetry as well as a rough pressure release surface that can predict the effects of rough surface scattering. During the field test, sound speed profile measurements were made, and surface wave buoy data was collected that provided realistic estimates of these features in the vicinity of the sensor system. Various geoacoustic bottom parameters were modeled in order to estimate the potential variability in transmission loss levels due to uncertainty in bottom type. Finally, models of merchant ship source levels were combined with the range of transmission loss predictions to develop estimates for received levels on the vector sensor system during the test. These estimates will then provide a guide during the post-processing of the data collected and may lead to improvements in source level modeling.

14. SUBJECT TERMS vector field, stability, low frequency, environmental variability	**15. NUMBER OF PAGES** 63
	16. PRICE CODE

17. SECURITY CLASSIFICATION OF REPORT	**18. SECURITY CLASSIFICATION OF THIS PAGE**	**19. SECURITY CLASSIFICATION OF ABSTRACT**	**20. LIMITATION OF ABSTRACT**
Unclassified	Unclassified	Unclassified	UU

NSN 7540-01-280-5500 Standard Form 298 (Rev. 2-89) Prescribed by ANSI Std. 239-18

THIS PAGE INTENTIONALLY LEFT BLANK

Approved for public release. Distribution is unlimited.

LOW-FREQUENCY ACOUSTIC VECTOR FIELD STABILITY IN THE PRESENCE OF ENVIRONMENTAL VARIABILITY

Fahmi Chandra Laksana
Lieutenant, Indonesia Navy
Diploma, Indonesian Naval Academy, 2007

Submitted in partial fulfillment of the
requirements for the degree of

MASTER OF SCIENCE IN ENGINEERING ACOUSTICS

from the

NAVAL POSTGRADUATE SCHOOL
September 2018

Approved by: Kevin B. Smith
Advisor

John E. Joseph
Second Reader

Oleg A. Godin
Chair, Engineering Acoustics Academic Committee

THIS PAGE INTENTIONALLY LEFT BLANK

ABSTRACT

The Department of Physics at the Naval Postgraduate School recently collected data from a low-frequency vector sensor system off the coast of Big Sur, California, in May 2018. During the test, signals from numerous surface craft were recorded. In this study, a numerical model was employed to estimate the vector field transmission loss at low frequency in order to estimate performance of the system during the test. In order to provide realistic ranges of values, the impact of environmental variability was examined and the primary factors affecting transmission loss were identified. The range-dependent environmental features included varying bathymetry as well as a rough pressure release surface that can predict the effects of rough surface scattering. During the field test, sound speed profile measurements were made, and surface wave buoy data was collected that provided realistic estimates of these features in the vicinity of the sensor system. Various geoacoustic bottom parameters were modeled in order to estimate the potential variability in transmission loss levels due to uncertainty in bottom type. Finally, models of merchant ship source levels were combined with the range of transmission loss predictions to develop estimates for received levels on the vector sensor system during the test. These estimates will then provide a guide during the post-processing of the data collected and may lead to improvements in source level modeling.

THIS PAGE INTENTIONALLY LEFT BLANK

TABLE OF CONTENTS

THIS PAGE INTENTIONALLY LEFT BLANK

LIST OF FIGURES

THIS PAGE INTENTIONALLY LEFT BLANK

LIST OF TABLES

THIS PAGE INTENTIONALLY LEFT BLANK

LIST OF ACRONYMS AND ABBREVIATIONS

2D	Two Dimensional
3D	Three Dimensional
AIS	Automatic Identification System
ASCII	American Standard Code for Information Interchange
CPA	Closest Point of Approach
IMO	International Maritime Organization
GPS	Global Positioning System
M/V	Motor Vessel
MMPE	Monterey Miami Parabolic Equation
NDBC	National Data Buoy Center
NOAA	National Oceanic and Atmospheric Administration
NPS	Naval Postgraduate School
PE	Parabolic Equation
RL	Receive Level
SL	Source Level
SSF	Split Step Fourier
SSP	Sound Speed Profile
TC-WAPE	Thomson Chapman Wide Angle Parabolic Equation
TL	Transmission Loss
UMPE	University of Miami Parabolic Equation
UTC	Universal Time Coordinated

THIS PAGE INTENTIONALLY LEFT BLANK

ACKNOWLEDGMENTS

I would like to express my highest gratitude to Allah Azza Wa Jalla, the almighty God, who makes beautiful things happen.

I thank my beloved wife, Hanum, and my son, Rafif, for their encouragement and for being cheerleaders every day. I thank my parents and sister for their support and prayers. I also appreciate my thesis advisors, Professor Kevin B. Smith and Professor John E. Joseph, for their patience and guidance during the process of working on this thesis.

Lastly, I would like to address my thanks to the Indonesia Endowment Fund for Education and the Indonesian Navy for the opportunity to see the other part of the world.

THIS PAGE INTENTIONALLY LEFT BLANK

I. INTRODUCTION

With the growing interest in acoustic vector field properties, more research is utilizing vector field measurements for a variety of purposes. This thesis attempts to illustrate potential instabilities in the vector field due to environmental uncertainty and range dependence. Both bathymetric changes and rough surface scattering are explicitly included in the solutions. Variations in bottom properties are also considered.

To analyze the stability of an acoustic vector field in shallow water, a numerical model that properly incorporates acoustic vector reciprocity can be used that demonstrates the impact of varying the environmental factors on the structure of vector field. To begin, three variables can be used as the environmental factors, namely sound speed profile, bottom properties and rough surface scattering. By varying one of the environmental factors at a time, a model result can be obtained and analyzed to find which environmental factor mostly affects the structure of the vector field.

Previously, Thomas J. Deal, in his thesis titled *Reciprocity in Vector Acoustics* (2017), derived the vector-scalar acoustic field reciprocity relationships. Unlike in pressure reciprocity, which generally relates to scalar fields and monopole sources and receivers, in vector field reciprocity, one cannot employ the same, simple reciprocal calculation for the pressure field due to the directionality of the orthogonal components of the velocity field. Deal also provided examples that showed the improper use of the scalar reciprocity relationship in the velocity fields fails to compute reciprocal structure properly.

The scenario to be modeled here is based upon a recent field test conducted by the Department of Physics of the Naval Postgraduate School off the coast of Big Sur, California, in May 2018. A low-frequency vector sensor system developed by GeoSpectrum Technologies, Inc., was deployed at a depth of 150 m and continuously recorded 4-channel acoustic vector sensor data for a period of approximately 4 days. During that time, AIS data was archived for post-processing reconstruction of sources of opportunity.

Using the proper acoustic vector field reciprocity relationships defined by Deal, this thesis focuses on qualitatively observing the impact on the stability of the acoustic vector field by the previously mentioned environmental factors. In Chapter II, this thesis will mostly discuss the theories used in environmental modeling, including a brief overview of the Monterey-Miami Parabolic Equation and the rough surface models. Chapter III will describe the environmental model results that include the analysis of environmental variability and Chapter IV will discuss the implications for measured acoustic vector field data of passing ships obtained during a recent sea test at the Naval Postgraduate School. The last chapter then concludes all the results and outlines the next prospective project.

II. THEORY

The theory of acoustic vector fields and the proper treatment of acoustic vector field reciprocity will be discussed in the first part of this chapter. In addition, this chapter also provides an overview of the Monterey Miami Parabolic Equation (MMPE) as the parabolic equation model used in this thesis and how it calculates the vector field. The last section of this chapter describes the rough surface models used in this simulation from a simple sinusoid to a wave buoy measured wave spectrum.

A. ACOUSTIC VECTOR FIELD

As a compressional wave, an acoustic wave produces disturbances within the fluid medium from its state of equilibrium. The interference that results from the constructive and destructive factors of sea surface and seabed interactions also affect the propagation of this acoustic wave. Along its propagating direction, this wave carries information about the environment in the components of acoustic pressure and particle velocity.

The acoustic pressure is the difference between the total pressure and the hydrostatic pressure, and it is the only quantity sensed by a traditional hydrophone. However, in the acoustic vector field, in addition to the pressure component, the 3D particle velocity components are required to fully describe the field (Mann, Tichy, & Romano, 1987). And to compute the particle velocity from pressure, one can evaluate the spatial gradient $\mathbf{v}(r,z) = \frac{1}{j\omega\rho_o}\nabla p(r,z)$ (Deal, 2017).

B. MONTEREY MIAMI PARABOLIC EQUATION (MMPE) MODEL

In the 1970s, Tappert (1974) introduced the use of the parabolic equation as an efficient means of predicting underwater acoustic propagation. Hardin and Tappert (1973) introduced the numerically stable and efficient split-step Fourier (SSF) algorithm to compute solutions of the pressure field. After that, many developments were made that improved this method, and the parabolic equation method has become one of the most popular techniques to solve range-dependent propagation problems in ocean acoustics.

In 1993, Smith and Tappert introduced the University of Miami Parabolic Equation (UMPE) model, which subsequently developed into the MMPE model in 2001 by Smith. The MMPE model was based on the approach used in the UMPE model, with some improvements introduced to increase solution accuracy.

The MMPE model considers the environmental factors such as range-dependent sound speed profiles, range-dependent bottom bathymetry and range-dependent bottom acoustic properties. Additionally, a range-dependent rough surface, range-dependent sub-bottom bathymetry and the associated sub-bottom acoustic properties can also be included (Tan & Leigh, 2018).

1. MMPE and Vector Field Reciprocity

Rayleigh, in his publication *The Theory of Sound* (1877), introduced the principle of pressure reciprocity. This principle can be succinctly defined by the equation

$$\frac{p_1(\mathbf{r}_2)}{\rho(\mathbf{r}_2)} = \frac{p_2(\mathbf{r}_1)}{\rho(\mathbf{r}_1)}, \tag{1}$$

which states that a source and receiver can be interchanged at positions $\mathbf{r}_1$ and $\mathbf{r}_2$, scaled by the local density, without a change in the observed field at the receiver. However, the equation above is only valid for omnidirectional sources and receivers. Thus, dealing with vector field reciprocity requires a more complex relationship. The reciprocity relationship for point sources can be stated as (Deal & Smith, 2018)

$$M_1 \frac{p_2(\mathbf{r}_1)}{\rho(\mathbf{r}_1)} - \boldsymbol{F}_1.\mathbf{v}_2(\mathbf{r}_1) = M_2 \frac{p_1(\mathbf{r}_2)}{\rho(\mathbf{r}_2)} - \boldsymbol{F}_2.\mathbf{v}_1(\mathbf{r}_2), \tag{2}$$

where M is the mass injection rate per unit volume and $\boldsymbol{F}$ is the vector directional force per unit volume, and the subscripts refer to the position of the source and the receiver. Now, consider $M_1 = 0$ and $\boldsymbol{F}_2 = 0$, which is consistent with a point source at position $\mathbf{r}_2$ and a dipole receiver at position $\mathbf{r}_1$. In this case, the reciprocal relationship is simplified to

$$-\boldsymbol{F}_1.\mathbf{v}_2(\mathbf{r}_1) = M_2 \frac{p_1(\mathbf{r}_2)}{\rho(\mathbf{r}_2)}. \tag{3}$$

The equation above allows the calculation of the received velocity component using the approach that is typically used to calculate received pressure. Unlike in standard pressure reciprocity, where a monopole source can be placed in the preferred spot and then one can evaluate the acoustic field everywhere for that source, applying the method of reciprocity to Equation 3 requires a two-step process. First, one must place a dipole source in a specific orientation at the reciprocal receiver location (e.g., where NPS deployed its vector sensor system), and the acoustic pressure field can be evaluated everywhere for that dipole source. (The pressure field represents the scalar field that would be measured by a monopole receiver, which is the type of reciprocal source we are assuming for distant merchant ship noise.) Then, divide the pressure calculated at each point by the density while neglecting the direction reversal. Since $|M_2| = \|\boldsymbol{F}_1\|$, then the equation will produce the amplitude of the velocity component that has the appropriate orientation as described in the first step. One can repeat this step to generate other velocity components for other dipole source orientations.

2. Basic MMPE Algorithm

Hardin and Tappert (1973) introduced the efficient SSF algorithm to evaluate solutions of the scalar (pressure) field, which later became the foundation of the basic MMPE algorithm. In the SSF algorithm, the surface is assumed to be a perfect reflecting boundary while the algorithm treats the bottom as an interface between the water column and another fluid medium defined by the geoacoustic properties of the sediment. Discontinuities in density are treated with smoothing functions and incorporated into an effective index of refraction.

Beginning with the wave equation for acoustic pressure $p(r,z)$, the linear Helmholtz equation takes the form

$$\frac{1}{r}\frac{\partial}{\partial r}\left(r\frac{\partial p}{\partial r}\right)+\rho\frac{\partial}{\partial z}\left(\frac{1}{\rho}\frac{\partial p}{\partial z}\right)+k_o^2 n^2 p=0\,, \tag{4}$$

where $n(r,z) = \frac{c_o}{c(r,z)}$ is the acoustic index of refraction, k_o is a reference acoustic wave number and $\rho(z)$ is the medium density as a function of depth. Defining the parabolic equation (PE) field function as

$$\psi(r,z) = \sqrt{\rho k_o r}\, p(r,z) e^{-ik_o r}, \tag{5}$$

the Helmholtz equation can be factored into incoming and outgoing solutions (Fishman, McCoy, & Wales, 1987), the outgoing part of which satisfies

$$\frac{\partial \psi}{\partial r} = -ik_o(1-Q)\psi \ . \tag{6}$$

In this equation, the PE differential operator is defined by

$$Q = \sqrt{N^2 + \frac{1}{k_o^2}\frac{\partial^2}{\partial z^2}}, \tag{7}$$

where *N* is an effective index of refraction that incorporates the density discontinuity at the water/bottom interface, according to (Smith, 2001)

$$N^2 = n^2 + \frac{1}{2k_0^2}\left[\frac{1}{\rho}\frac{\partial^2 \rho}{\partial z^2} - \frac{3}{2}\left(\frac{1}{\rho}\frac{\partial \rho}{\partial z}\right)^2\right]. \tag{8}$$

The Thomson and Chapman (1983) wide angle parabolic equation (TC-WAPE) approximation is used in the MMPE model, such that

$$Q = \sqrt{1+\varepsilon'+\mu} \approx \sqrt{1+\mu} + \sqrt{1+\varepsilon'} - 1, \tag{9}$$

where

$$\varepsilon' = N^2 - 1 \text{ and } \mu = \frac{1}{k_o^2}\frac{\partial^2}{\partial z^2}. \tag{10}$$

The MMPE employs a centered step SSF scheme, such that solutions are marched forward in range according to

$$\psi(r+\Delta r,z)=e^{-ik_o\frac{\Delta r}{2}U_{op}(r+\Delta r,z)}\times IFFT\left\{e^{-ik_o\Delta r\hat{T}_{op}(k_z)}\times FFT\left[e^{-ik_o\frac{\Delta r}{2}U_{op}(r,z)}\times\psi(r,z)\right]\right\}, \quad (11)$$

where

$$T_{op}\left(\frac{\partial^2}{\partial z^2}\right)=1-\sqrt{1+\mu}=1-\sqrt{1+\frac{1}{k_o^2}\frac{\partial^2}{\partial z^2}}\Rightarrow\hat{T}_{op}\left(k_z\right)=1-\sqrt{1-\frac{k_z^2}{k_o^2}} \quad (12)$$

and

$$U_{op}(r,z)=\sqrt{1+\varepsilon'}=1-N^2=1-n^2-\frac{1}{2k_o^2}\left[\frac{1}{\rho}\frac{\partial^2\rho}{\partial z^2}-\frac{3}{2}\left(\frac{1}{\rho}\frac{\partial\rho}{\partial z}\right)^2\right]. \quad (13)$$

The starting field definition for a monopole source at depth z_s is defined in MMPE by (Smith, 2001)

$$\hat{\psi}_m\left(k_z\right)=-2i\sqrt{\frac{iR_o}{2\pi k}}\sin\left(k_{z,}z_s\right)\left(1-\frac{k_z^2}{k^2}\right)^{\frac{1}{4}}e^{ik_z\frac{dz}{2}}. \quad (14)$$

This is normalized to give 0 dB transmission loss at range 0. The output of the 2D MMPE model produces pressure, and horizontal and vertical components of particle velocity.

To generate vertical dipole sources for acoustic vector field reciprocal calculations, a secondary point source that is shifted by 180 degrees is introduced, such that (Deal, 2017)

$$\hat{\psi}_v\left(k_z\right)=-2i\sqrt{\frac{iR_o}{2\pi k}}\left[iA_z\sin\left(k_z\left[z_s+\Delta z\right]\right)-iA_z\sin\left(k_z\left[z_s-\Delta z\right]\right)\right]\left(1-\frac{k_z^2}{k^2}\right)^{\frac{1}{4}}e^{ik_z\frac{dz}{2}}, \quad (15)$$

where

$$A_z=\frac{i}{2k\Delta z}. \quad (16)$$

Hence, if Equation 15 is used in place of Equation 14, the model will produce pressure, radial velocity and vertical velocity for a vertical dipole source.

Similarly, for a horizontal dipole source the starting field is defined as (Deal, 2017)

$$\begin{aligned}\hat{\psi}_h(k_z) = -2i\sqrt{\frac{iR_o}{2\pi k}}[&A_o \sin\left(k_z\left[z_s - 4\Delta z\right]\right) \\ &+ A_1 \sin\left(k_z\left[z_s - 2\Delta z\right]\right) + A_2 \sin\left(k_z z_s\right) + A_3 \sin\left(k_z\left[z_s + 2\Delta z\right]\right) \\ &+ A_4 \sin\left(k_z\left[z_s + 4\Delta z\right]\right)]\left(1 - \frac{k_z^2}{k^2}\right)^{\frac{1}{4}} e^{ik_z\frac{dz}{2}}\end{aligned} \tag{17}$$

where

$$A_k = \frac{(-1)^k n!}{k!(n-k)!}; k = 0...n, \tag{18}$$

and k is the zero-based array element index.

3. Rough Surface Modeling with MMPE

The sea surface is often approximated as a pressure release boundary in the calculation of underwater acoustic propagation. By defining the range-dependent sea surface boundary according to

$$z = \eta(r), \tag{19}$$

the equation defining the condition of the pressure release boundary becomes

$$\psi(z = \eta(r), r) = 0. \tag{20}$$

In the SSF approach, this boundary condition is satisfied by employing the image ocean odd symmetry of the field, which now takes the form

$$\psi(-z + 2\eta(r), r) = -\psi(z, r). \tag{21}$$

In contrast, the even symmetry of the environment complies with the expected relationship

$$U_{op}(-z + 2\eta(r), r) = U_{op}(z, r). \tag{22}$$

Application of the parabolic equation to both the real and image oceans then leads to

$$\frac{\partial \psi}{\partial r} = -ik_o(T_{op} + U_{op})\psi \qquad z > \eta(r) \quad \text{Real Ocean} \tag{23}$$

$$\frac{\partial \psi}{\partial r} + 2\frac{\partial \eta}{\partial r}\frac{\partial \psi}{\partial z} = -ik_o(T_{op} + U_{op})\psi \quad z < \eta(r) \quad \text{Image Ocean} \tag{24}$$

As shown by Tappert and Nghiem-Phu (1985), these equations can be combined into a single parabolic equation by introducing the field transformation

$$\tilde{\psi}(z,r) = \begin{cases} \psi(z,r) & z > \eta(r) \text{ Real Ocean} \\ e^{-i2k_o\frac{\partial \eta}{\partial r}}\psi(z,-z+2\eta(r)) & z < \eta(r) \text{ Image Ocean} \end{cases}. \tag{25}$$

This leads to a single PE of the form

$$\frac{\partial \tilde{\psi}}{\partial r} = ik_o(\tilde{T}_{op} + \tilde{U}_{op})\tilde{\psi}\,, \tag{26}$$

where the operators now take the form

$$\tilde{\hat{T}}_{op}(k_z) = \begin{cases} \hat{T}_{op}(k_z), & z > \eta(r) \text{ Real Ocean} \\ \hat{T}_{op}(k_z), & z < \eta(r) \text{ Image Ocean} \end{cases}, \tag{27}$$

and

$$\tilde{U}_{op}(z,r) = \begin{cases} U_{op}(z,r) & z > \eta(r) \text{ Real Ocean} \\ U_{op}(-z+2\eta(r),r) - 2\frac{\partial^2 \eta}{\partial r^2}(z-\eta) & z < \eta(r) \text{ Image Ocean} \end{cases}. \tag{28}$$

4. Description of Rough Surface Models

a. Simple Sinusoidal Surface Wave

The simple sinusoidal surface assumes that the surface wave is defined only by a wave height and wave length. Although this type of surface never exists in the real ocean, it provides the fundamental view of how the field is affected by rough surface scattering. In this case, the surface displacement is defined by

$$\eta(r) = A\cos(k_s r)\,, \tag{29}$$

where A is the wave height and k_s is the surface wave number, related to the surface wavelength by $k_s = 2\pi/\lambda$.

b. Pierson-Moskowitz Wave Spectrum

This type of spectrum is often characterized by the assumption if the wind blew steadily for a long period over a large surface area, the waves would eventually come into equilibrium with the wind (Pierson & Moskowitz, 1964). Figure 1 depicts various synoptically chosen spectra at different wind speeds introduced by Moskowitz.

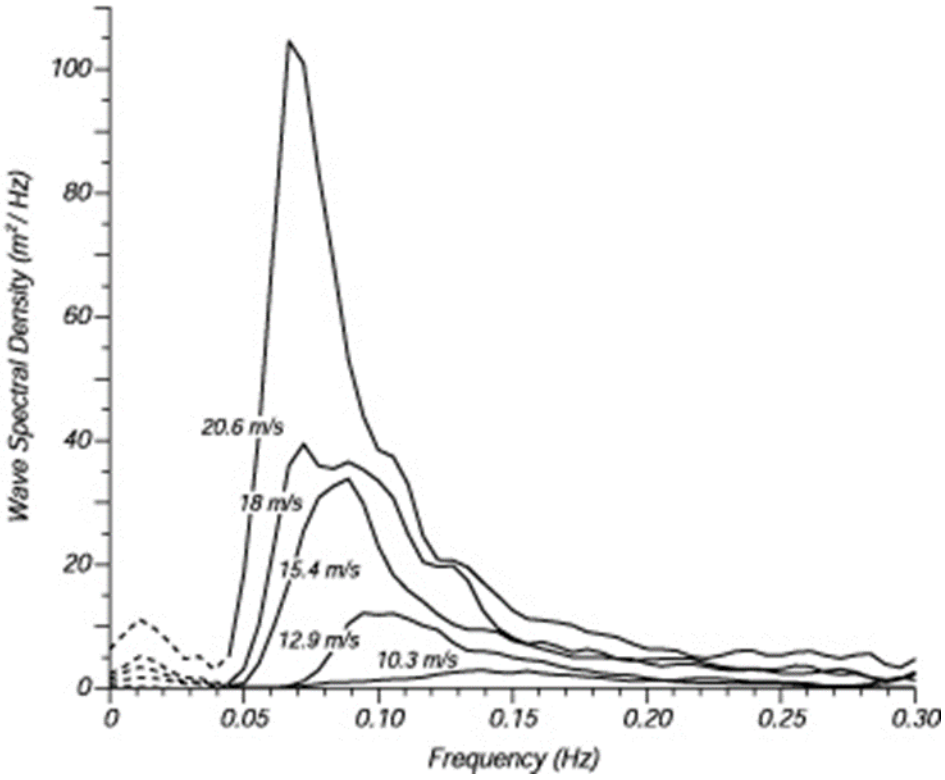

Figure 1. Graphs of the synoptically chosen spectrum. Source: Moskowitz (1964).

Figure 1 shows that different wind speeds will create different wave spectra, which are then empirically defined by

$$S(\omega) = \frac{\alpha g^2}{\omega^5} \exp\left(-\beta \left(\frac{\omega_o}{\omega} \right)^4 \right). \tag{30}$$

Since $\omega_o = g / U_{19.5}$, another form of the equation above is

$$S(\omega) = \frac{\alpha g^2}{\omega^5} \exp\left(-\beta \frac{g^4}{\omega U_{19.5}{}^4} \right), \tag{31}$$

where $\omega = 2\pi f$, f is the surface wave frequency (in Hz), $\alpha = 8 \times 10^{-3}$ and $\beta = 0.74$ are constants (Pierson & Moskowitz, 1964), $g = 9.8 \, m/s^2$ is the acceleration due to gravity, and $U_{19.5}$ is the wind speed at the elevation level of 19.5 m above the sea surface.

This equation for a rough sea surface spectrum can then be used to generate random realizations with the appropriate spectral content. Random surfaces $\eta(k_r)$ are generated from the user defined spectrum using a normal distribution where $\rho, \sigma \in N(0,1)$. Then

$$\hat{V}_o(k_r) = \frac{1}{\sqrt{2}} \left[p(k_r) + i\sigma(k_r) \right] \sqrt{\frac{S_{PM}(k_r)}{2} \Delta k}, \tag{32}$$

$$\hat{V}(k_r) = \frac{1}{\sqrt{2}} \left[\hat{V}_o(k_r) + \hat{V}_o^*(-k_r) \right], \tag{33}$$

and finally a realization is computed from the real part of

$$\eta(r) = IFFT\left\{ \hat{V}(k_r) \right\}. \tag{34}$$

c. Wave Buoy Measured Wave Spectrum

In order to construct a proper wave buoy measured wave spectrum, one can obtain the raw spectral data from oceanographic buoys, provided at www.ndbc.nooa.gov. The raw spectral data file contains pairs of data points that describe frequency and magnitude in hour intervals over a span of 45 days. In a manner similar to the creation of a rough surface realization using the Pierson-Moskowitz spectrum, this user-defined spectrum can be read by MMPE to create properly scaled realizations consistent with the buoy measurements.

THIS PAGE INTENTIONALLY LEFT BLANK

III. ENVIRONMENTAL MODEL

As described in a previous chapter, the variability of 3 environmental features are used to analyze the stability of the acoustic vector field in our test environment. To effectively measure which factors produce the largest effect on the structure of the vector field, those factors are varied one by one.

A. SOUND SPEED PROFILE VARIATIONS

A total of five sound speed profiles were collected from five different points. As shown in Figure 2, the center point was located near the deployment site of the vector sensor system, at the coordinate 36.3833 N and 121.9925 W, while the others were located on the north, south, west and east of the center point at approximately 1 km range. Figure 3 depicts the average sound speed profiles from these five points.

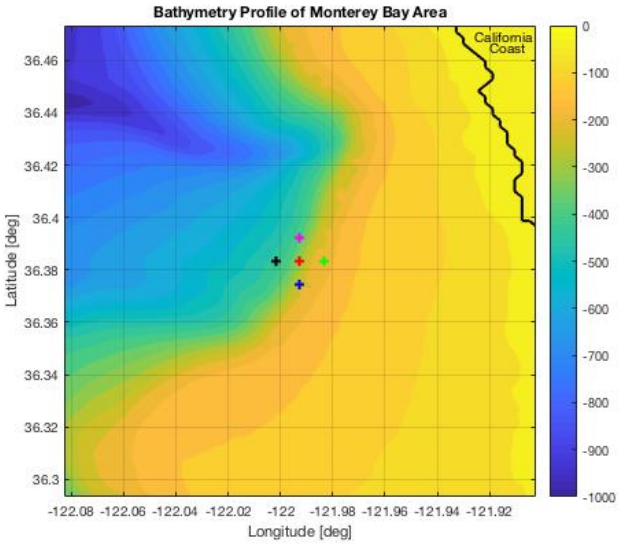

Figure 2. The bathymetry map showing the locations for SSP data collection represented by the five colored dots.

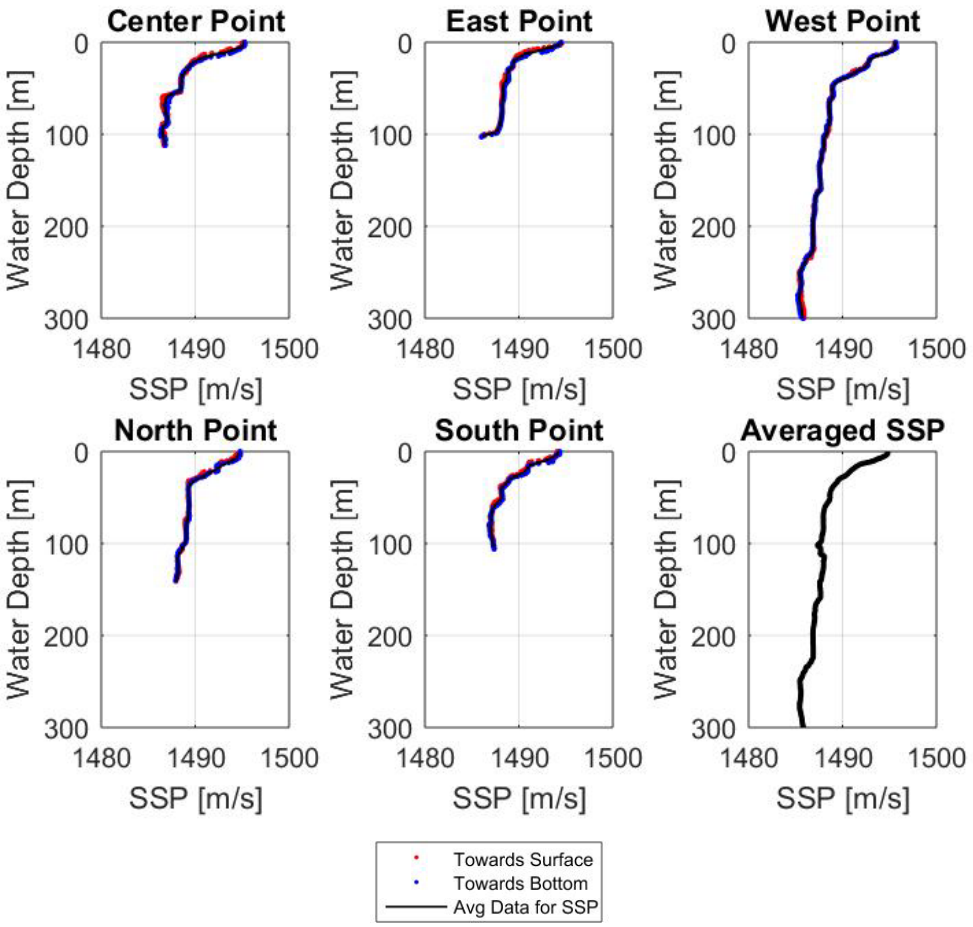

Figure 3. Sound speed profiles.

The field solutions were computed along four different bathymetric lines: from center to north, center to east, center to south, and center to west. The bathymetry along each track was extracted from the bathymetry data obtained from the Department of Oceanography of the Naval Postgraduate School. This data was gridded on a 100 m x 100 m mesh with a total size of 361x721, for a total extent of 36.1 km west to east and 72.1 km south to north. The depth of the sensor system at deployment was between 150-160 m. Based on the GPS position of the boat near the time of deployment, and the bathymetry database described, the source location was defined to be at 36.3833N and 121.9925W. A Matlab script was used to extract bathymetry data along tracks to the north, east, south, and west of this position, which was then stored as an ASCII input file to MMPE. Plots of these bathymetry lines are depicted in Figure 4.

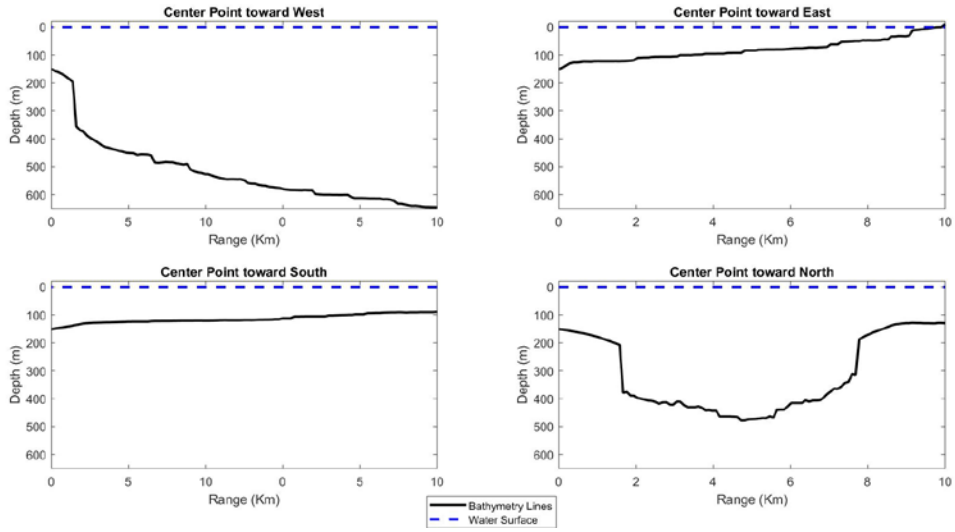

Figure 4. Bathymetry lines.

Prior to running a simulation scenario, a set of geoacoustic parameters are defined as follows in Table 1. Because much of the interest will relate to observations of passing merchant traffic during the May test, most of the analysis will focus on the range-dependent propagation from the center to the west towards the open ocean. Numerical solutions were computed out to a range of 10 km in all scenarios, but only the solutions showing propagation to the west will be presented for brevity.

Table 1. Bottom properties for SSP variation.

Sound speed $\left(m/s\right)$	1684.4
Density $\left(g/cm^3\right)$	1.91
Gradient $\left(1/s\right)$	0
Attenuation $\left(dB/m/kHz\right)$	0.391

In order to examine variable propagation effects due to the sound speed profile, a set of profiles taken during the test at the west, center and east points were utilized as input to the model in both range-dependent and range-independent combinations (only out to a range of 1 km from the sensor's location, then range-independent at longer ranges). The following images show the model results for an omnidirectional source and environment previously defined. The modeled source is placed at the receiving system's location at range 0 and depth 150 m (1 m off the bottom). The results are then treated as reciprocal calculations out in range to all locations where actual sources (e.g., merchant ships) may be operating. All calculations presented here were computed at a single frequency of 25 Hz. Variability is introduced through changes in the sound speed profiles, as indicated in the caption.

As observed in Figure 5, the field structure qualitatively looks similar for each different SSP. Thus no matter which SSP is used, the model shows a similar field structure with a small difference in transmission loss for a low frequency source at any range or depth. Even if two different SSPs are used in a range-dependent manner, the model solutions maintain a similar structure. To demonstrate that the SSP variability also does not have a significant impact on the velocity field structures, Figures 6 and 7 display the results when a horizontal and a vertical dipole source are used (reciprocal to what would be received from a point source out in range). In addition, both Figures 6 and 7 suggest that, for a 25 Hz source, SSP variability does not have a significant impact on the vector field stability.

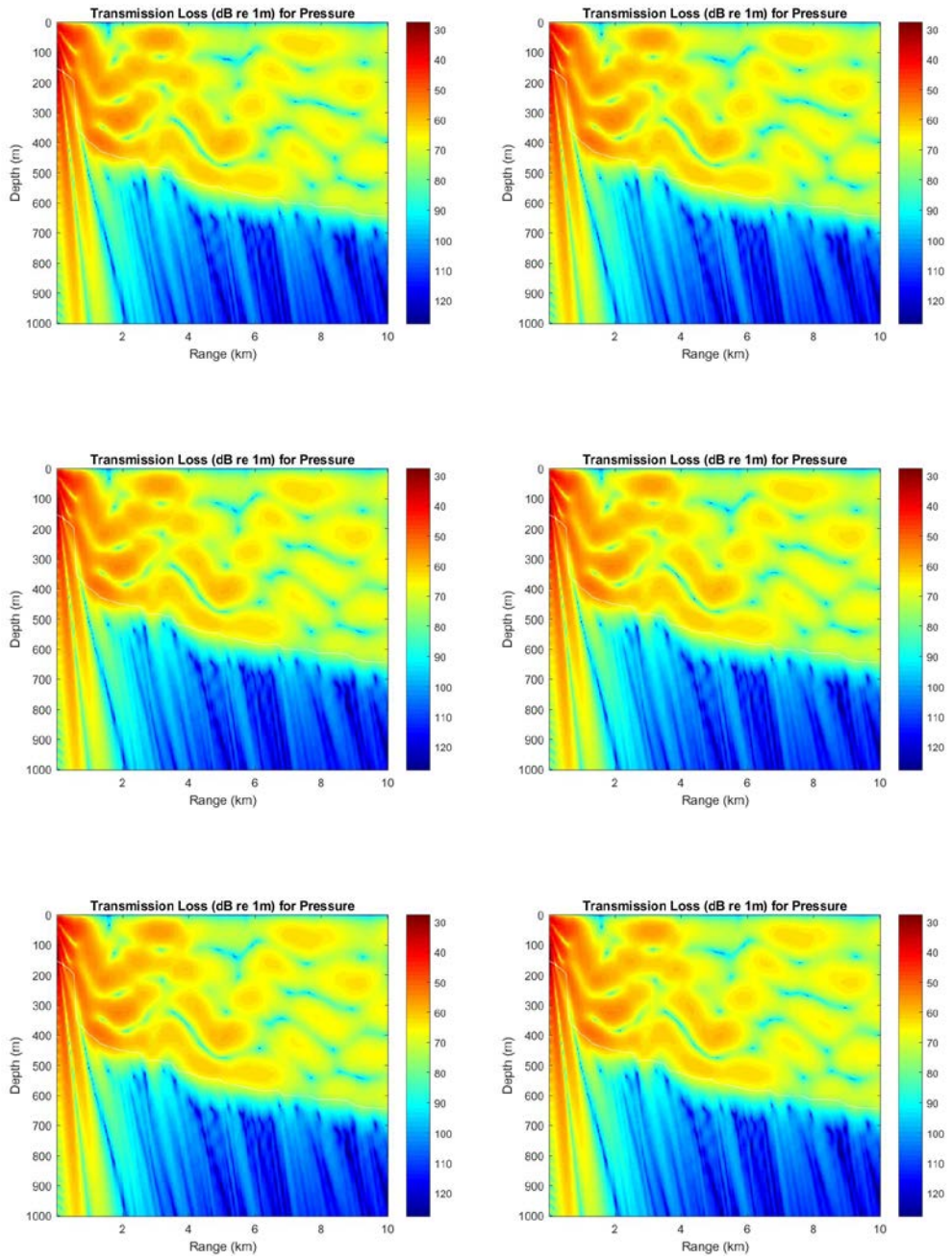

Figure 5. Transmission loss (dB re 1 m) for an omnidirectional source and by using center point SSP (top left), east point SSP (top right), west point SSP (middle left), averaged SSP (middle right) and center-west point SSP (bottom left), center-east point SSP (bottom right) to check for range dependency.

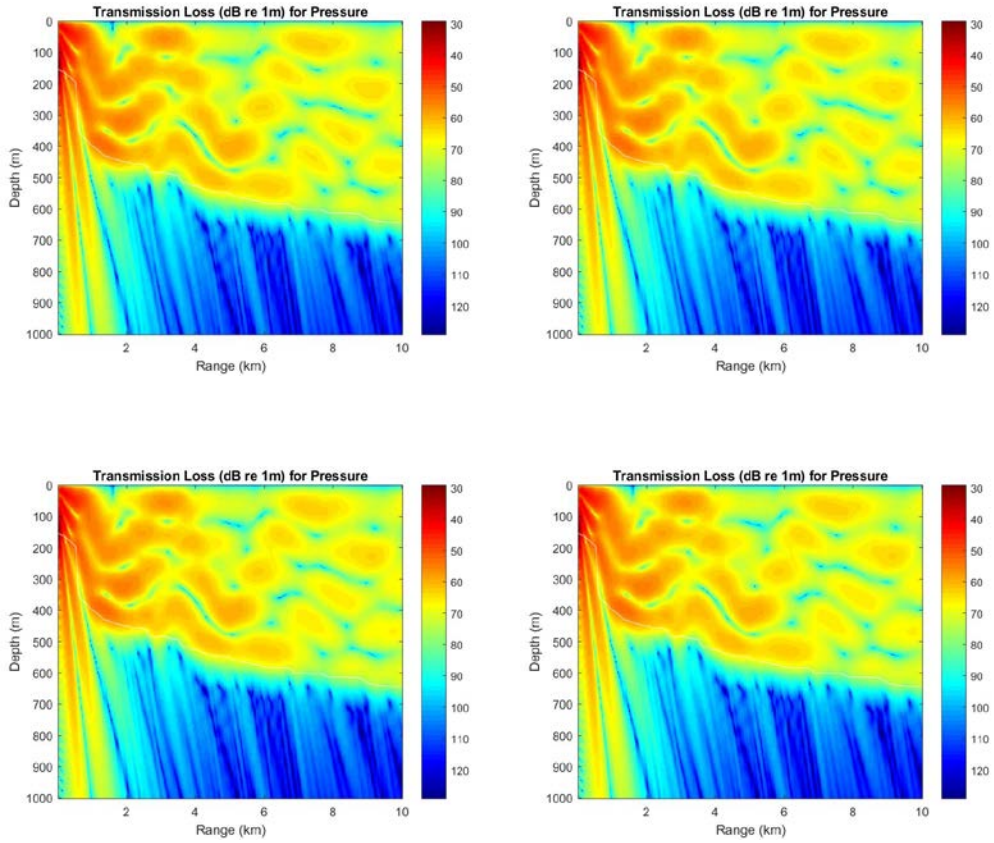

Figure 6. Transmission loss (dB re 1 m) for a horizontal dipole source and using center point SSP (top left), east point SSP (top right), west point SSP (bottom left) and averaged SSP (bottom right).

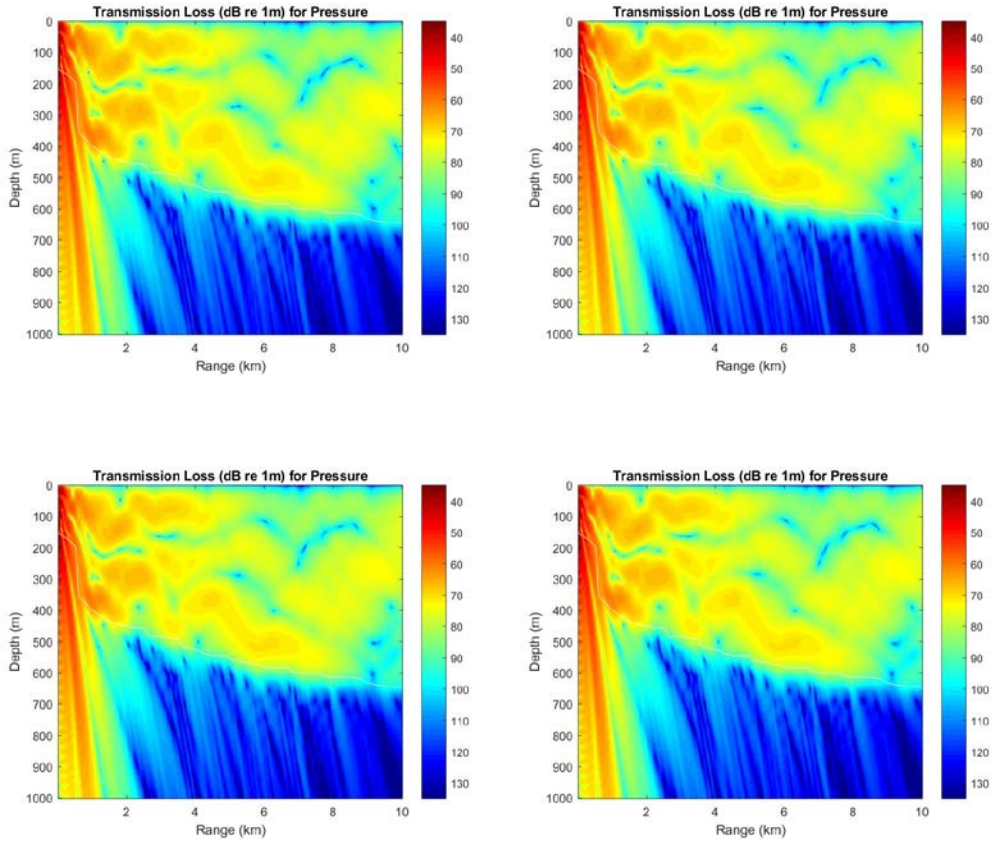

Figure 7. Transmission loss (dB re 1 m) for a vertical dipole source and using center point SSP (top left), east point SSP (top right), west point SSP (bottom left) and averaged SSP (bottom right).

B. BOTTOM VARIATIONS

To evaluate the impact of bottom properties on vector field stability, another set of parameters are introduced. Table 2 shows the list of parameters that characterize each variation of geoacoustic properties, namely sound speed, sound speed gradient, density and attenuation loss.

Table 2. Parameters used for bottom properties variation.

	Sound speed $\left(m/s\right)$	Sound speed gradient $\left(1/s\right)$	Density $\left(g/cm^3\right)$	Attenuation loss $\left(dB/m/kHz\right)$
Muddy sand	1684.4	0.0	1.911	0.391
Muddy sand 2	1650.0	1.0	1.8	0.4
Muddy sand 3	1650.0	0.0	1.8	0.4
Muddy sand 4	1650.0	0.0	2.008	1.01
Coarse sand	1708.5	0.0	2.008	1.01
Coarse sand 2	1700.0	1.0	2.0	0.8
Coarse sand 3	1708.5	0.0	1.5	0.2
Coarse sand 4	1600.0	0.0	2.008	1.01
Soft sand	1600.0	0.0	1.5	0.2
Soft sand 2	1600.0	0.0	2.008	0.2
Soft sand 3	1600.0	0.0	1.5	1.01

1. Bottom Sound Speed and Gradient

To evaluate vector field stability against ocean bottom sound speed variations, the characteristics of both “Coarse sand 3” and “Soft sand” are used. As seen in the table, the only difference between those two characteristics are the value of sound speed while the values of other parameters remain the same.

Figure 8 shows that as the sediment sound speed decreases, the field structure starts to show increases of TL at some points. When the sediment sound speed is higher, TL is somewhat reduced and more fine-scale structure is observed. This is consistent with an increase in higher order modes that can propagate energy down the waveguide due to the

faster bottom. However, much of the field structure remains similar and TL levels remain within 5 dB of each other.

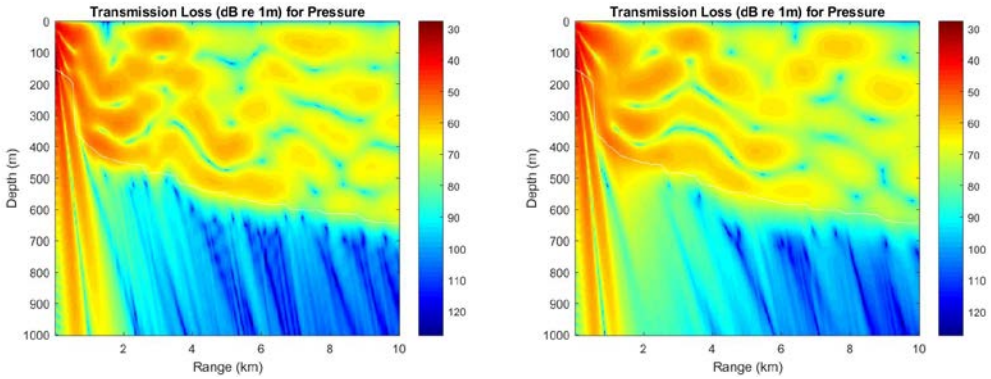

Figure 8. Transmission loss (dB re 1 m) of an omnidirectional source for coarse sand 3 with higher sound speed (left) and soft sand with lower sound speed (right).

Next, “Muddy sand 2” and “Muddy sand 3” are used to evaluate the vector field stability against an ocean bottom sound speed gradient variation. As in the previous scenario, the only different parameter is the value of the sound speed gradient.

As shown in Figure 9, the structure of the TL shows minor changes as the value of sound speed gradient increases from 0 /s to 1 /s, especially at longer ranges. However, this variation in bottom sound speed gradient appears to have less impact than the bottom sound speed at the interface.

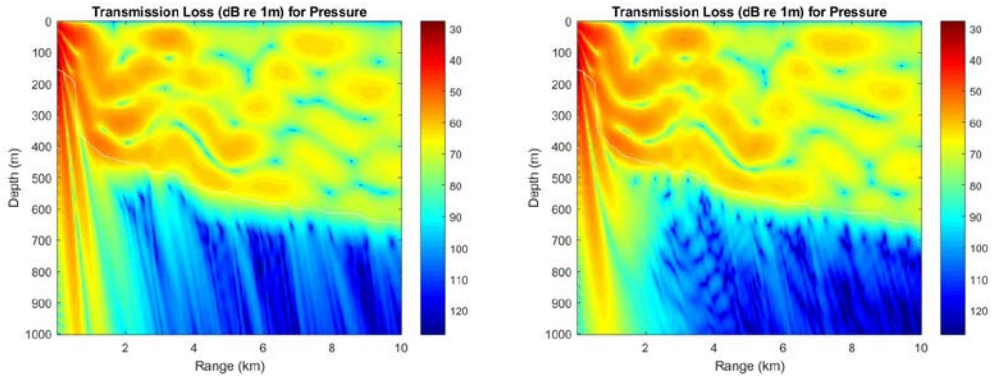

Figure 9. Transmission loss (dB re 1 m) of an omnidirectional source for muddy sand 3 with 0/s gradient (left) and muddy sand 2 with 1/s gradient (right).

2. Bottom Density

To see the effect of a bottom density variation, the characteristics of "Soft sand" and "Soft sand 2" are used. According to the table, the only difference between these types of soft sand is the value of their densities. As shown in Figure 10, the structure of the vector field is almost identical when the density increases from 1.5 g/cm^3 to 2.008 g/cm^3, suggesting much less sensitivity to variations in bottom density.

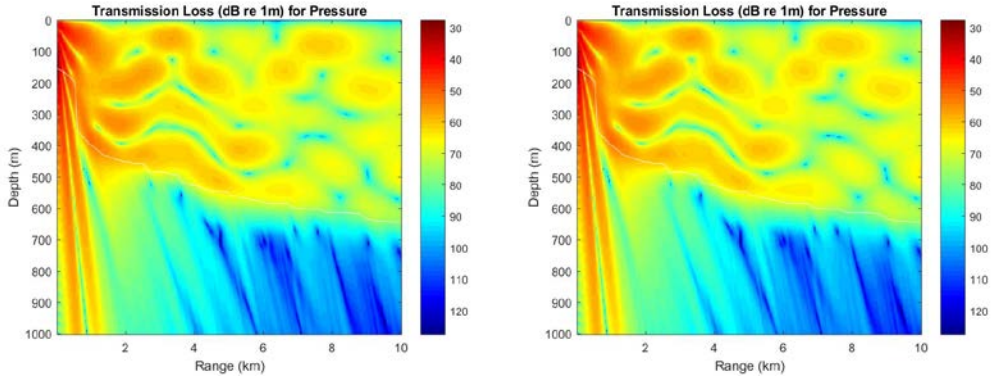

Figure 10. Transmission loss (dB re 1 m) of an omnidirectional source for soft sand with 1.5 gr/cm^3 density (left) and soft sand 2 with 2.008 gr/cm^3 density (right).

3. Bottom Attenuation

The last variable bottom property considered is the bottom attenuation or, more explicitly, the compressional attenuation. In this case, the characteristics of “Soft sand” and “Soft sand 3” are used which clearly are different in their values of bottom attenuation. According to Table 3, the attenuation loss of soft sand is 0.2 dB/m/kHz while soft sand 3 has 1.01 dB/m/kHz for its bottom attenuation loss.

As may have been expected, Figure 11 shows that as the bottom attenuation loss increases, the transmission loss increases. However, this does not significantly affect the vector field structure. Since the sound speed and density are the same (same real impedance), then the increased bottom loss will simply result in an overall loss in the propagation of energy while the structure of the individual propagating modes will remain mostly unchanged.

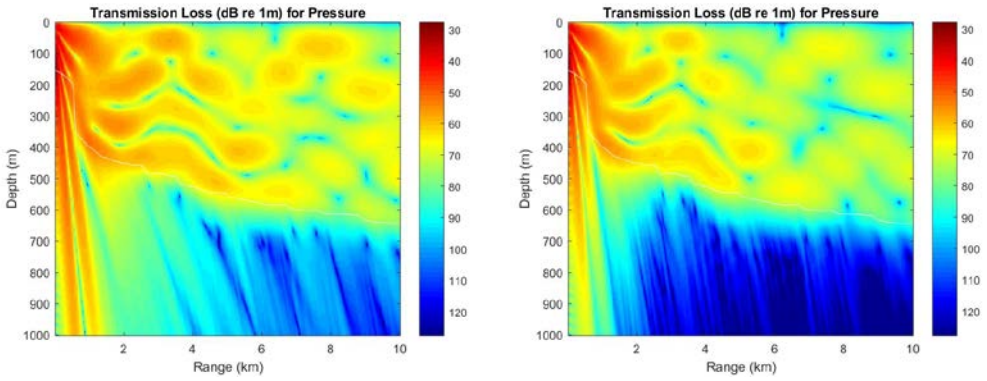

Figure 11. Transmission loss (dB re 1 m) of an omnidirectional source for soft sand with 0.2 dB/m/kHz bottom attenuation (left) and soft sand 3 with 1.01 dB/m/kHz (right).

It should be noted that similar analyses were conducted for both horizontal and vertical dipole source calculations. The general observations of the impacts of those environmental variations were the same, and so the figures are not presented here for the sake of brevity.

C. SURFACE ROUGHNESS VARIATIONS

There are three scenarios considered for surface roughness variation. Namely, a simple sinusoidal wave, a Pierson-Moskowitz wave spectrum, and a wave buoy measured wave spectrum based on buoy data from the period of the data collection event. Each surface model has its own characteristics, as defined in the introductory chapters.

1. Sinusoidal Wave

The scenario for the sinusoidal wave is the simplest scenario. In this scenario, the wave is only defined by the wave height and the wavelength, thus the wave characteristic is regular and analytic. For all cases presented here, the surface wavelength is defined as 100 m. The surface wave height is then varied from 2 m to 4 m to 6 m.

As shown in Figure 12, the transmission loss increases at longer ranges as the wave height is increased from 2 m to 6 m, although the general structure is the same. At 6 m, there is noticeable small-scale fluctuations in the field, as well. This may be expected at 6 m wave height, where the wave height is quite large and surface slopes approach values of 20 deg. Thus, the sound wave is more diffusely scattered by the surface and results in higher transmission loss throughout the field.

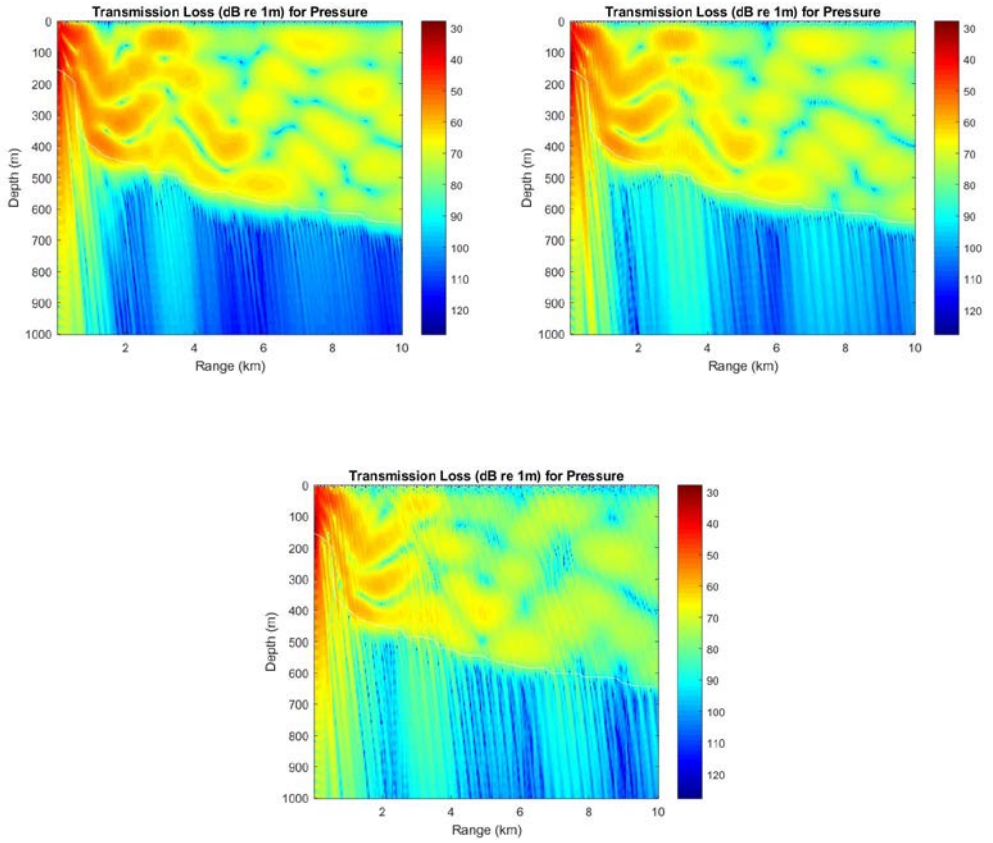

Figure 12. Transmission loss (dB re 1 m) of an omnidirectional source with coarse sand bottom profile for sinusoidal wave and applying 2 m wave height and 100 m wave length (top left), 4 m wave height and 100 m wave length (top right) and 6 m wave height and 100 m wave length (bottom).

2. Pierson-Moskowitz Wave Spectrum

As described in Chapter II, the general idea of the Pierson-Moskowitz spectrum is the equilibrium condition as the result of the wind steadily blowing over a large surface area. In this sub section, the wind speed is set at 10 knot, 20 knot and 40 knot for each respective scenario, with rms roughness values of 0.474, 1.428, and 4.776 m, respectively.

As shown in Figure 13, the vector field structure starts to exhibit significant, small-scale (< 200 m) fluctuations as the wind speed increases to 40 knots. This result is consistent with the previous analyses by Tan and Leigh (Tan & Leigh, 2018). In that work, it was shown that surface scattering from PM spectra tend to become pronounced for wind

speeds > 15 knots. However, even with these fluctuations, the general structure and TL levels in the field appear mostly unaffected.

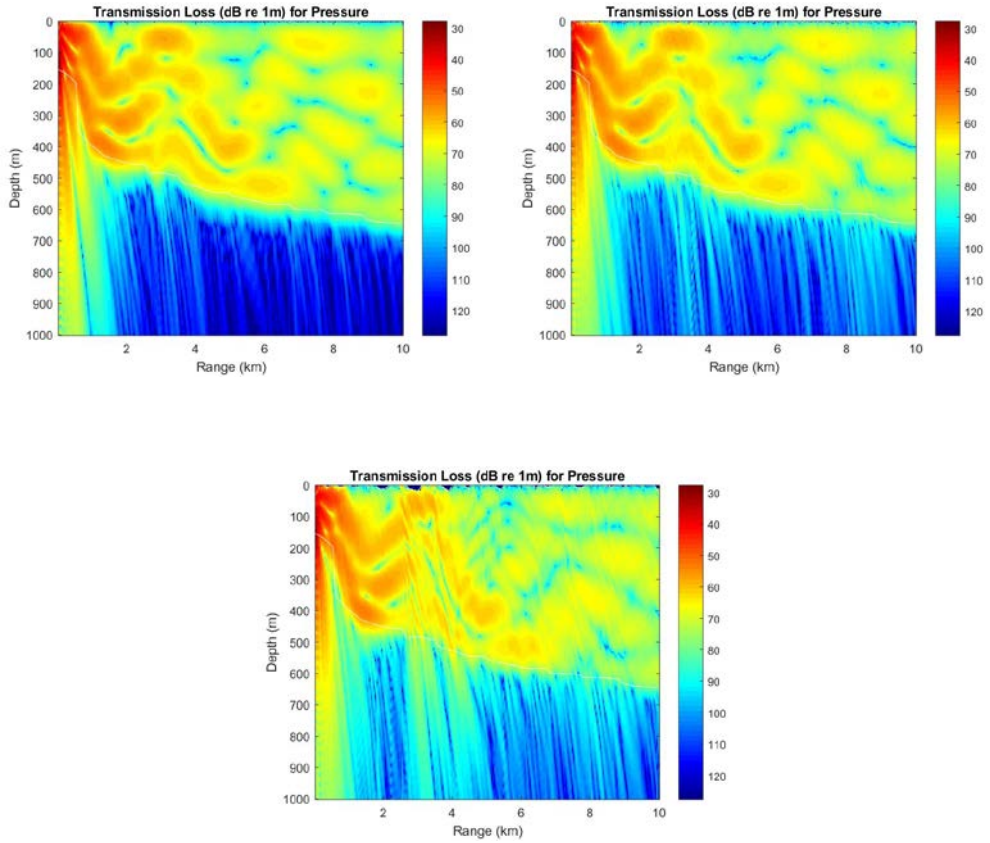

Figure 13. Transmission loss (dB re 1 m) of an omnidirectional source with coarse sand bottom profile for Pierson-Moskowitz spectrum when applying 10 knot of wind speed (top left), 20 knot of wind speed (top right), and 40 knot of wind speed (bottom).

Figures 14 and 15 show the corresponding results for the horizontal and vertical dipole sources, respectively. As seen with the omni-directional source, the overall field structures remain reasonably consistent with the introduction of the small scale fluctuations due to scattering, while the general TL levels remain mostly unaffected.

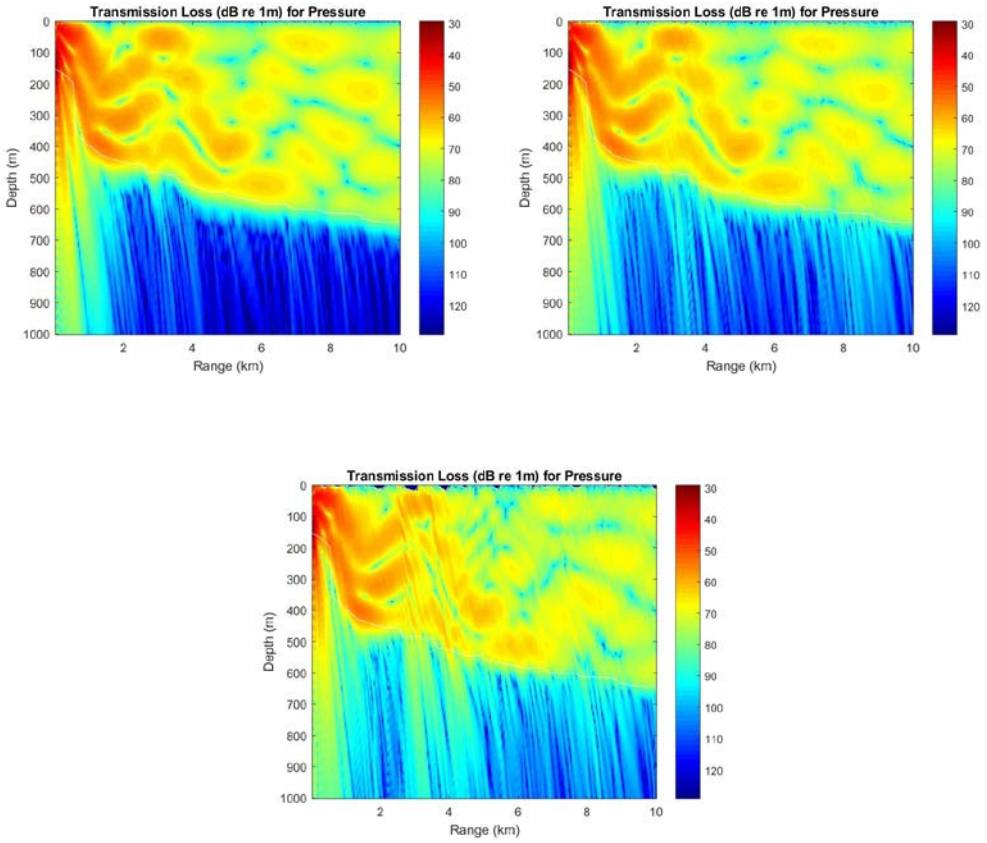

Figure 14. Transmission loss (dB re 1 m) of a horizontal dipole source with coarse sand bottom profile for Pierson-Moskowitz spectrum when applying 10 knot of wind speed (top left), 20 knot of wind speed (top right), and 40 knot of wind speed (bottom).

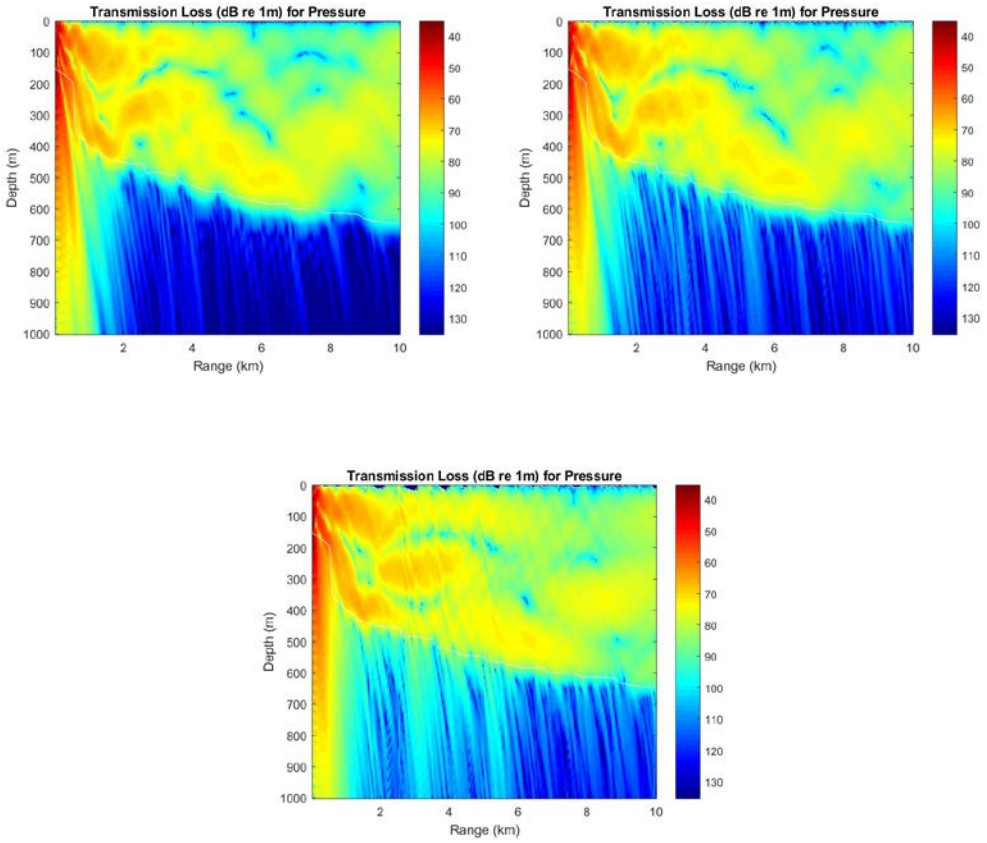

Figure 15. Transmission loss (dB re 1 m) of a vertical dipole source with coarse sand bottom profile for Pierson-Moskowitz spectrum when applying 10 knot of wind speed (top left), 20 knot of wind speed (top right), and 40 knot of wind speed (bottom).

3. Wave Buoy Measured Wave Spectrum

The wave buoy measured wave spectrum scenario uses the archived historical data obtained from the NOAA National Data Buoy Center of a wave buoy, number 46239 located off Point Sur, on the date of May 15, 2018. The figure below depicts the surface roughness realizations generated from the data at different times of day.

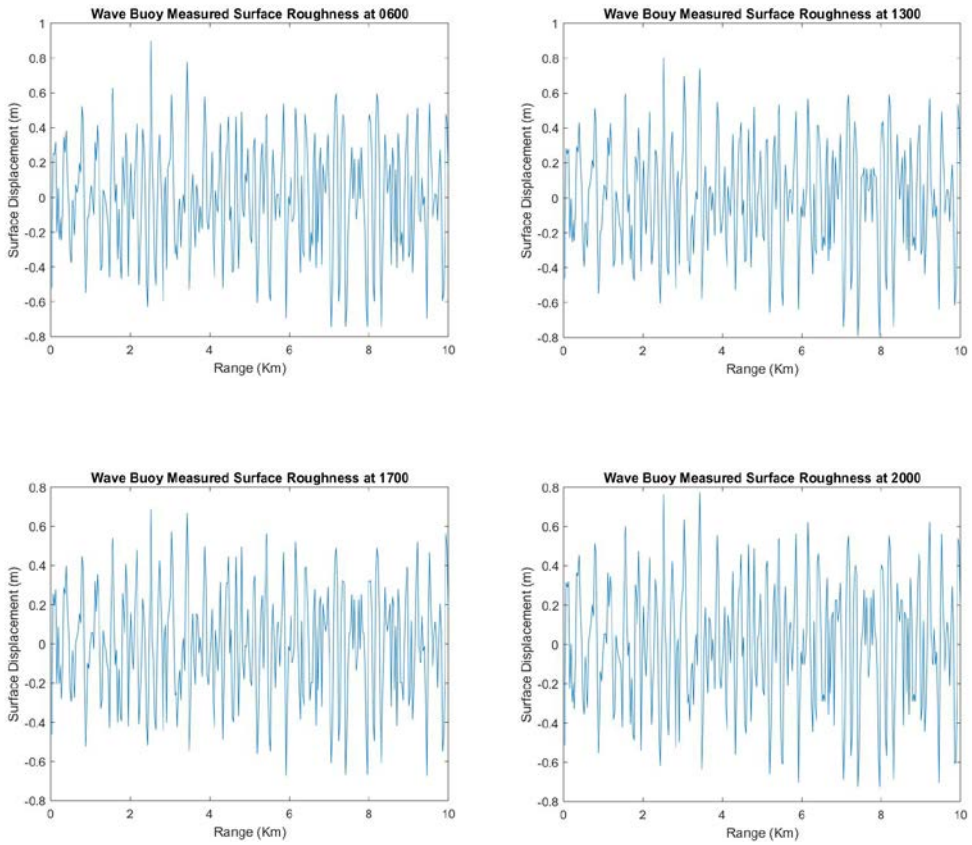

Figure 16. Wave buoy measured surface roughness generated from the data obtained from wave buoy number 46239 on May 15, 2018.

Figure 17 shows that both the TL levels and the structure of the field tend to be unaffected. Figure 16 shows that the maximum surface wave displacement never exceeds 1 m, and thus does not appear to have any noticeable impact on the results. This is consistent with the results from the Pierson-Moskowitz analysis for wind speeds < 10 kts.

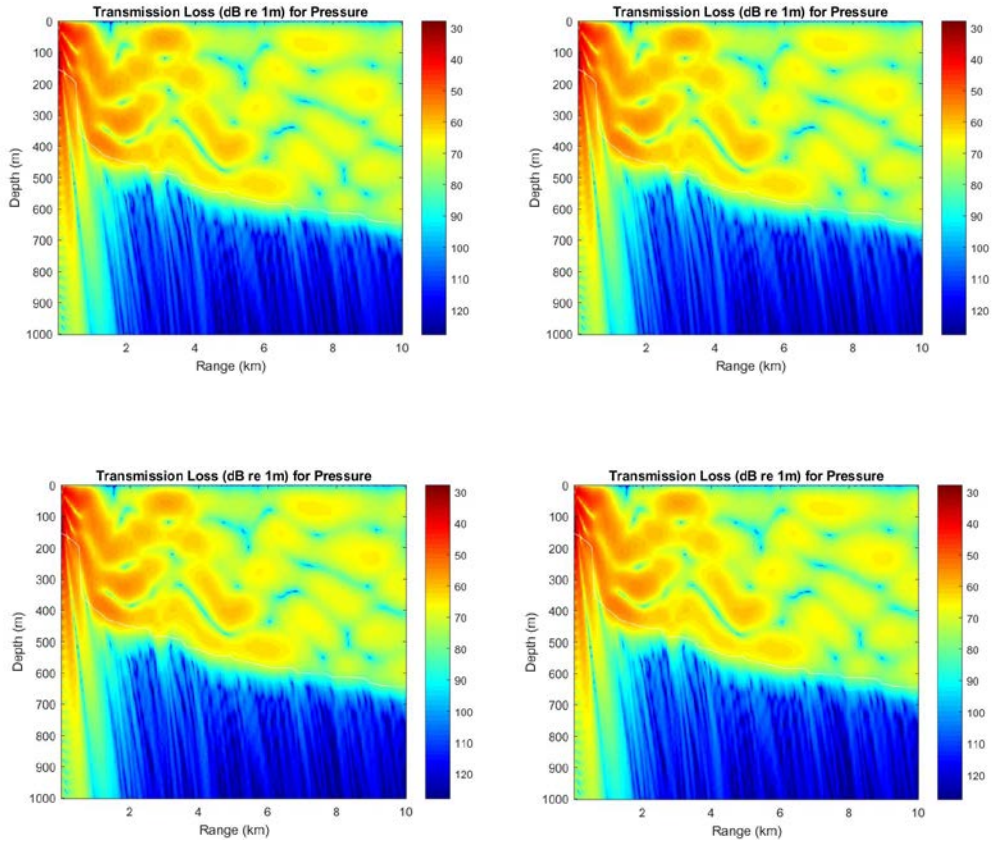

Figure 17. Transmission loss (dB re 1 m) of an omnidirectional source with coarse sand bottom profile for wave buoy measured wave spectrum obtained on May 15th 2018 at 0600 (top left), 1300 (top right), 1700 (bottom left) and 2000 (bottom right).

IV. IMPLICATION FOR MEASURED DATA OF PASSING SHIP

During the deployment of the GeoSpectrum system in May 2018, AIS data of ships passing the vicinity of the testing area were recorded. This chapter discusses the calculated approximation of source level using formula derived by Ross (1976) and subsequent analysis by McKenna, Ross, Wiggins, and Hildebrand (2012). These references allow us to estimate source levels for passing ships, and thereby predict estimates for received levels (*RL*) on the sensor system from the simple sonar equation

$$RL = SL - TL\,. \tag{35}$$

A. SHIP INFORMATION

Based on the AIS data, several ships are passing in the vicinity of the deployment area. One of the ships that approached quite close to the deployment point was the M/V Jubilant. Figure 18 depicts the range of the ship relative to the vector sensor recording system per 30-minute intervals. At the closet point of approach (CPA), the M/V Jubilant was at a range of 2.195 km to the sensor system. At the time that it was approximately due west of the sensor system, the range to the M/V Jubilant was also 2.195 km. This range will be used to estimate the *TL* from the previous calculations to estimate *RL* on the sensor system.

However, the name Jubilant is used by many ships. Therefore, to obtain more information about the tracked ship, it is necessary to know what type of the ship the Jubilant is. Using the historical tracking data provided by FleetMon.com, and by observing the ship traffic on May 15, 2018, from Lopez Point to Cypress Point, California, new information about the M/V Jubilant with a call sign WDI 6026 is obtained. Figure 19 shows the historical tracking data. Since this information concurs with data provided by the AIS recording system, the M/V Jubilant is positively confirmed to be the ship recorded by the AIS recording system.

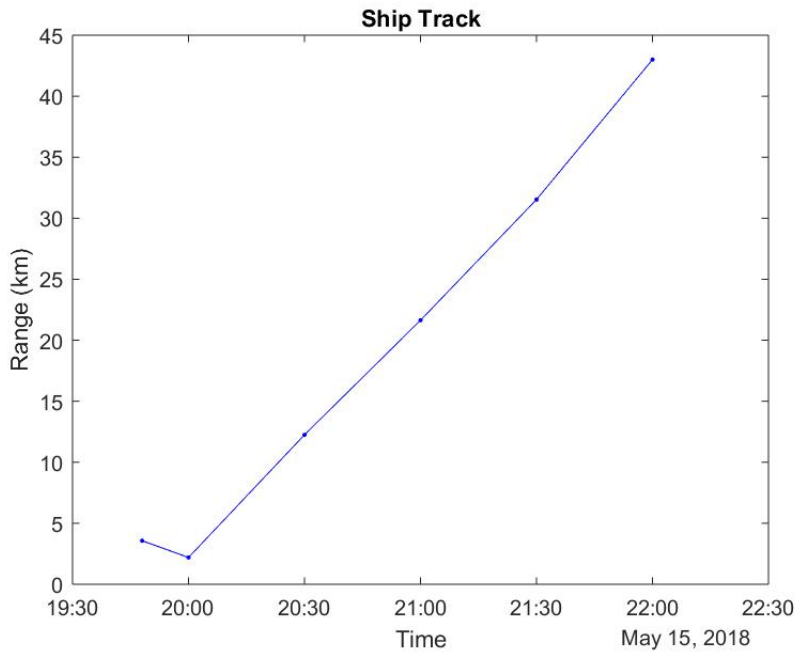

Figure 18. Range of Jubilant relative to the recording system.

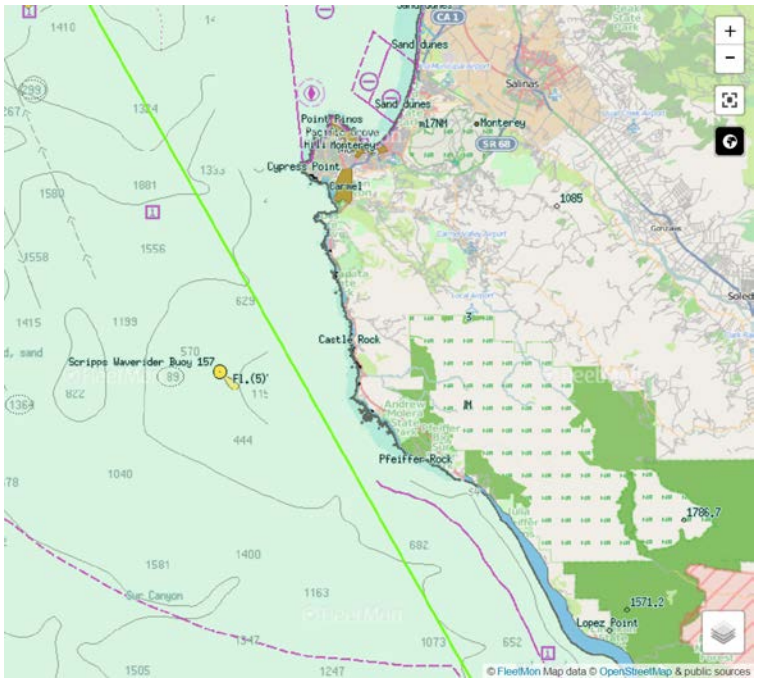

Figure 19. Ship track of Jubilant sailing in the vicinity of Lopez Point to across Cypress Point, California. Source: https://www.fleetmon.com/vessels/jubilant_0_10562864/#tab-historical-track.

B. SOURCE LEVEL ESTIMATION

Ross (1976) developed an equation to estimate the source level of a ship with an assumption that the propeller is the dominant source of the radiated noise. However, the result of the equation is only valid for a source with 100 Hz frequency or above. The form of the equation is

$$SL = 154 + 60\log\left(\frac{S}{10}\right) + 9\log(DT) - 20\log(f), \tag{36}$$

where SL is the source level (in dB re 1 μPa, 1 Hz, 1 yard), S is the speed of the ship in knots, DT is the ship displacement in tons, and f is the frequency measured in Hz.

In Tonnage Guide 1 published by United States Coast Guard (2009), the hull volume of a ship can be approximated by using the following equation

$$V = L \times B \times D \times F, \tag{37}$$

where V is volume, B is beam and D is draft in meters, while F is the shape factor with a value of 0.67 for powerboat, ship shape and circular hull. Then, multiplying the volume displacement with sea water density should provide the weight displacement. For the values of the M/V Jubilant provided in Table 3, the ship's displacement is estimated at 293 tons. Figure 20 then depicts the result of Equation 36 for the frequency range 100–10000 Hz when the ship is moving at a speed of 20.4 knots.

Table 3. Dimension of M/V Jubilant

Length (m)	31.4
Beam (m)	6.86
Draft (m)	1.98

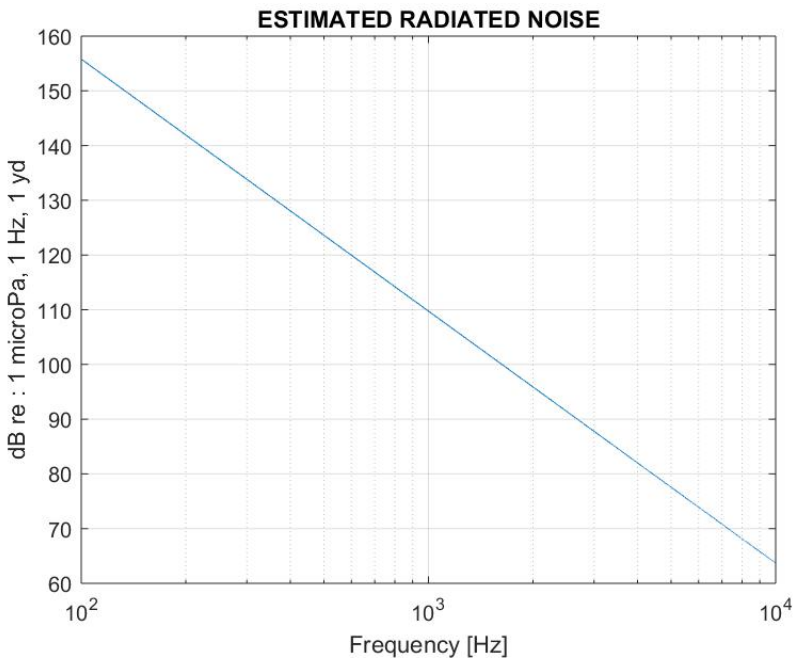

Figure 20. Estimated radiated noise of M/V Jubilant

At frequencies below 100 Hz, the analysis by McKenna et al. (2012) suggests that the *SL* rolls off to a relatively constant level. Therefore, we may expect the *SL* of the M/V Jubilant to lie somewhere between 150 and 160 dB (re 1μPa, 1Hz, 1yd). (Note that the difference between a source level referenced at 1 yd or 1 m is less than 1 dB, so this range of *SL* estimates remains the same.) At a range of 2.2km, the previous model results suggest shallow sources would have *TL* values of approximately 65 – 75 dB (re 1m). Combining these results, we estimate that the *RL* on the system at the time the M/V Jubilant is due west of the sensor should be in the range 75 - 95 dB (re 1μPa, 1Hz). Note from the structure of the *TL* fields previously analyzed, there is a minimum near the surface at a range of about 3 km. It would be expected that ships passing to the west of the system at ranges around 3 km would provide the largest received signals.

Differences from this in the processed data (yet to be completed) could be due to various factors. However, at these ranges, there were not significant variations observed in *TL* levels due to the various environmental factors considered. Thus, the most likely factor

contributing to differences would be an incorrect approximation of the source level. The measured data may then be used to improve the estimation of *SL* from passing ships.

C. SOURCE LEVEL ESTIMATION OF A LARGER SHIP

Even though M/V Jubilant seemed to be a promising ship to be identified, to fully utilize the information provided in the paper by McKenna et al. (2012), a larger merchant ship contact is desired. Therefore, an extended bathymetry line was extracted from the bathymetry data to provide a simulation that covers a larger range up to 15 km from the center point as shown in Figure 21.

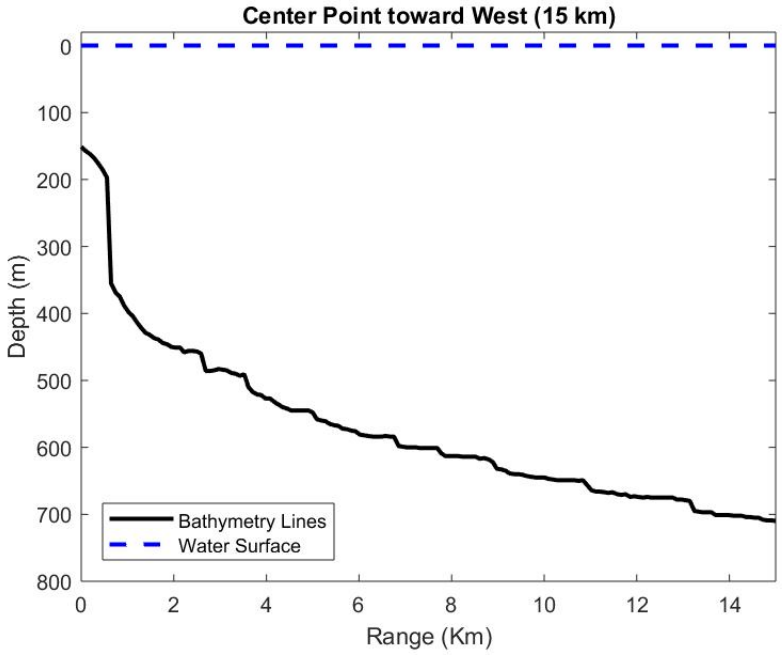

Figure 21. Extended 15 Km bathymetry line

In 15 km radius from the center point toward the west direction, Cap Jackson, a large container vessel registered in Singapore with IMO number 9484560, is one of the promising targets. Table 4 below describes the dimension of M/V Cap Jackson.

Table 4. Dimension of M/V Cap Jackson

Length (m)	264
Beam (m)	32
Draft (m)	12.3
DWT (tonnes)	59336

As in the previous target analysis, historical tracking data provided by FleetMon.com is used to confirm if M/V Cap Jackson passed across the research area during the deployment of the GeoSpectrum system. Figure 22 positively confirms that M/V Cap Jackson was navigating to the southeast across the research area at an average speed of 9.1 knots on May 17th 2018, while Figure 23 shows the range of M/V Cap Jackson relative to the sensor system. During that time, the CPA range to the sensor system was 13.95 km and CPA time was at 2200 (UTC). The range at which the M/V Cap Jackson was precisely due west of the sensor was 14.81 km, and this range will be used to estimate the transmission loss.

By using the TL levels predicted in Figure 25, with the surface roughness realization obtained from NDBC - NOAA as depicted in Figure 24, the estimated TL at the time M/V Cap Jackson was sailing precisely to the west of the sensor was between 80-90 dB (re 1m). McKenna, et al (2011) estimates the SL at 1 m of a ~50000-ton gross tonnage container ship with speed 20.6 knots to be approximately 185 dB (re 1μPa, 1m, 1Hz). Using this SL value, the estimated RL should fall between 95 and 105 dB (re 1μPa, 1Hz). This range of values will be used as a guide in subsequent processing of the data collected during the May 2018 trials.

Figure 22. Ship track of M/V Cap Jackson navigating in the vicinity of Cypress Point to across Point Sur, California. Source: https://www.fleetmon.com/vessels/cap-jackson_9484560_2077828/#tab-historical-track.

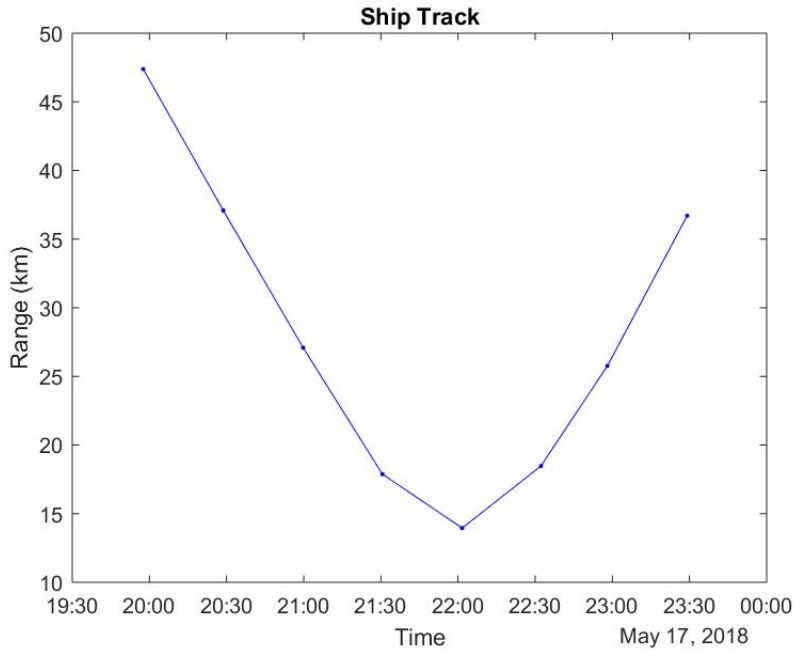

Figure 23. Range of M/V Cap Jackson relative to the recording system.

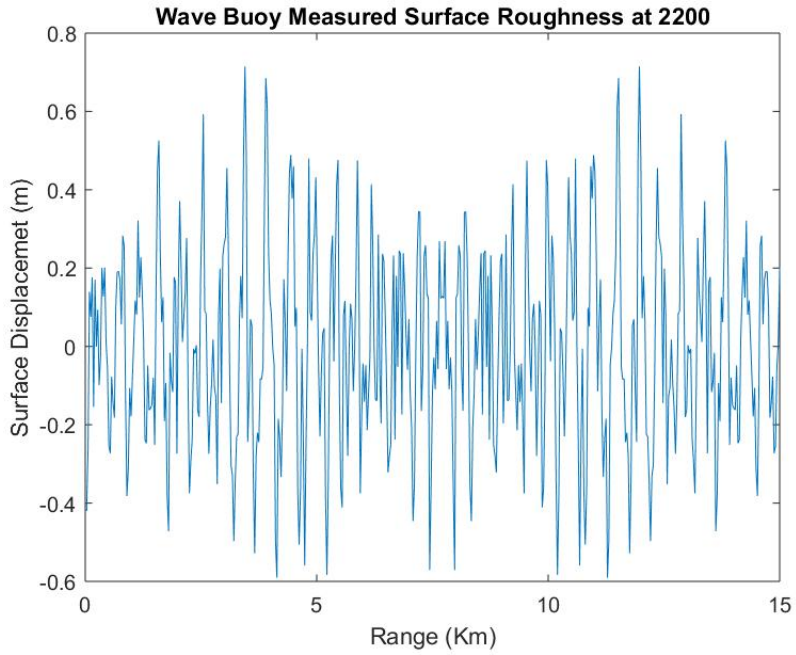

Figure 24. Wave buoy measured surface roughness generated from the data obtained from wave buoy number 46239 on May 17, 2018.

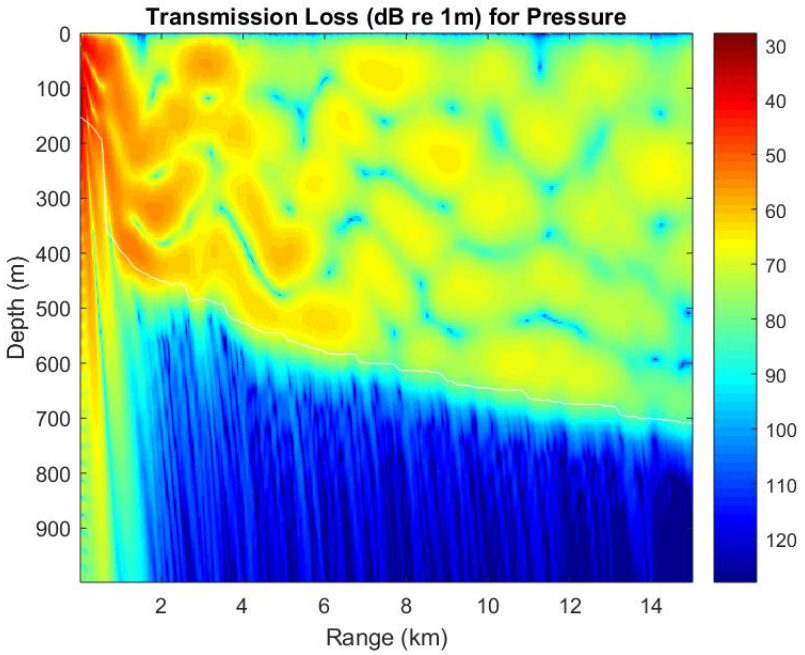

Figure 25. Transmission loss (dB re 1 m) of an omnidirectional source with coarse sand bottom profile for wave buoy measured wave spectrum obtained on May 17, 2018.

V. CONCLUSION

In this thesis, the effects of some environmental factors on the stability of the acoustic vector field at low frequency were investigated. The general area of interest was consistent with the deployment of a vector sensor system in relatively shallow water near the continental shelf break off the coast of Big Sur, California, in May 2018. Model results were generated from the MMPE model and considered variations in sound speed profile (based on measured data), bottom geoacoustic properties (based on estimates of sediment type in the region), and rough surface scattering (based on various surface types, including surface spectra collected by a nearby buoy).

Based on the analysis of the MMPE calculations, variations in sound speed profile do not appear to have a significant impact on the structure of the acoustic vector field and its transmission loss at low frequencies, even when a range-dependent SSP is applied to the calculation. This observation was also true of calculations for both horizontal and vertical dipole sources (reciprocal evaluations of the horizontal and vertical velocity fields of the vector sensor system).

For variations in bottom geoacoustic properties, both sound speed and the sound speed gradient of the sediment had a noticeable influence on the predicted acoustic vector field, particularly beyond a few km. As anticipated, higher sound speeds or gradients caused more energy to be reflected from the bottom, thereby increasing the overall energy observed at longer ranges. The effects were most pronounced in the energy levels rather than the interference structure of the field itself. In contrast, the bottom density had the least effect on both the transmission loss and the structure of the field. Not surprisingly, bottom attenuation had the greatest impact on the long-range transmission of energy due to its effect on bottom reflections. The bottom profile with higher attenuation loss reflected less energy compared to the one with lower attenuation. However, the structures of the field remained very similar.

Variations in surface roughness had a minimal impact on the stability of the vector field at the frequencies examined. For instance, the sinusoidal wave surface roughness with

amplitude displacements of 2 m, 4 m and 6 m produced nearly identical results to the case with a flat surface. Similarly, if the Pierson-Moskowitz wave spectrum was applied, the result depended on the wind speed. The higher wind speed produced more transmission loss and more small-scale structure, even though qualitatively the average structure of the vector field components remained similar. For the results obtained using the wave buoy measured wave spectrum, there was no significant difference on either the structure of acoustic vector field or the transmission loss.

Because the structure of the field remained relatively stable in the presence of all of these variations, and the dominant effect was a change in the levels of energy transmission, this suggests that known sources may provide a means of confirming some bottom loss estimates. Thus, the goal of Chapter IV was to develop estimates for some approximate source levels of passing merchant ships that were likely detected during the May 2018 test. Conversely, if there is confidence in the characterization of the bottom properties, these calculations could serve as a means of estimating the actual source levels of the ships detected by the system.

Many uncertainties may affect the results of such a calculation. For instance, the bottom profile used assumes a single bottom type, whereas a layer of softer sediment may overlay a harder sub-bottom structure. The sounds transmitted by passing merchant ships are also assumed to be omnidirectional, which may not be a valid assumption. However, despite the uncertainties, the results presented here suggest that, if some of these unknowns can be ascertained by other means, the field has significant stability at low frequency that could support the estimation of other parameters.

LIST OF REFERENCES

Deal, T.J. (2017). *Reciprocity in vector acoustics* (Master's thesis). Retrieved from http://hdl.handle.net/10945/52968

Deal, T.J., & Smith, K.B. (2017). Reciprocity relationship in vector acoustics and their application to vector field calculations. *The Journal of the Acoustical Society of America, 142*(2), 523–529. doi:10.1211/1.4996458

Fishman, L., McCoy, J.J., & Wales, S.C. (1987). Factorization and path integration of the Helmholtz equation: Numerical algorithms. *The Journal of the Acoustical Society of America, 81*(5), 1355–1376. doi:10.1211/1.394542

Hardin, R.H, & Tappert, F.D. (1973). Applications of the split-step Fourier Method to the numerical solution of nonlinear and variable coefficient wave equations. *SIAM Rev., 15*(2), 423. doi:10.1137/1015060

Mann, J.A., Tichy, J., & Romano, A.J. (1987). Instantaneous and time-averaged energy transfer in acoustic fields. *The Journal of the Acoustical Society of America, 82*(1), 17-30. doi:10.1121/1.395562

McKenna, M.F., Ross, D., Wiggins, S.M., & Hildebrand, J.A. (2012). Underwater radiated noise from modern commercial ships. *The Journal of the Acoustical Society of America, 131*(1), 92–103. doi:10.1121/1.3664100

Moskowitz, L. (1964). Estimates of the power spectrums for fully developed seas for wind speeds of 20 to 40 knots. *Journal of Geophysical Research, 69*(24), 5161–5179. doi:10.1029/JZ069i024p05161

Pierson, W.J., & Moskowitz, L. (1964). A proposed spectral form for fully developed wind seas based on the similarity theory of S.A. Kitaigorodskii. *Journal of Geophysical Research, 69*(24), 5181–5190. doi:10.1029/JZ069i024p05181

Rayleigh, J., & Lindsay, R. (1945). *The theory of sound* (2nd ed. rev. and enl.). New York, NY: Dover publications.

Ross, D. (1976). *Mechanics of underwater noise*. New York, NY: Pergamon Press.

Smith, K.B., & Tappert, F.D. (1993). *UMPE: The University of Miami parabolic equation model. Version 1.0.* Retrieved from http://www.dtic.mil/dtic/tr/fulltext/u2/a270570.pdf

Smith, K.B. (2001). Convergence, stability, and variability of shallow water acoustic predictions using a split-step Fourier parabolic equation model. *The Journal of Computational Acoustics, 9(1),* 243–285.

Tan, Y.L., & Leigh, G.H.V. (2018). *Higher-order boundary and rough surface treatment of the MMPE model in the evaluation of scattering effects* (Master's thesis). Retrieved from http://hdl.handle.net/10945/58373

Tappert, F.D. (1974). Parabolic equation method in underwater acoustics. *The Journal of the Acoustical Society of America*, *55*(S1), S34-S34. doi:10.1121/1.1919661

Tappert, F.D., & Nghiem-Phu, L. (1985). A new split-step Fourier algorithm for solving the parabolic wave equation with rough surface scattering. *The Journal of the Acoustical Society of America*, *77*(S1), S101-S101. doi:10.1121/1.2022130

Thomson, D.J., & Chapman, N.R. (1983). A wide-angle split step algorithm for the parabolic equation. *The Journal of the Acoustical Society of America*, *74*(6), 1848–1854. doi:10.1121/1.390272

United States Coast Guard. (2009). *Simplified measurement - tonnage guide 1*. Washington, DC: Author. Retrieved from https://www.dco.uscg.mil/Portals/9/DCO%20Documents/Marine%20Safety%20Center/Tonnage/Tonnage%20Guide%201%20-%20Simplified%20Measurement.pdf?ver=2017-06-09-123757-680

INITIAL DISTRIBUTION LIST

1. Defense Technical Information Center
   Ft. Belvoir, Virginia

2. Dudley Knox Library
   Naval Postgraduate School
   Monterey, California